CHEMISTRY OF MATERIALS

pubs.acs.org/cm

Article

Highly Active Rhenium-, Ruthenium-, and Iridium-Based Dichalcogenide Electrocatalysts for Oxygen Reduction and Oxygen Evolution Reactions in Aprotic Media

Leily Majidi, Zahra Hemmat, Robert E. Warburton, Khagesh Kumar, Alireza Ahmadiparidari, Liang Hong, Jinglong Guo, Peter Zapol, Robert F. Klie, Jordi Cabana, Jeffrey Greeley, Larry A. Curtiss,* and Amin Salehi-Khojin*

Cite This: *Chem. Mater.* 2020, 32, 2764–2773

Read Online

ACCESS | Metrics & More | Article Recommendations | Supporting Information

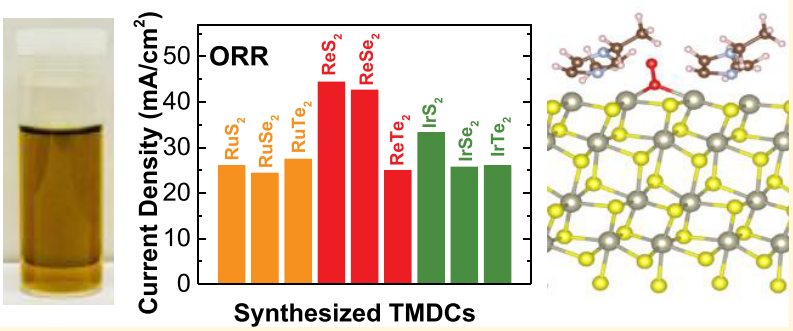

ABSTRACT: Transition metal dichalcogenides (TMDCs) have garnered much attention recently due to their remarkable performance for different electrochemical systems. In this study, we report on the synthesis and catalysis of less studied TMDC nanoflakes (NFs) with a design space comprised of three transition metals (rhenium, ruthenium, and iridium) and three chalcogens (sulfur, selenium, and tellurium) for the oxygen reduction and evolution reactions (ORR and OER) in an aprotic hybrid electrolyte containing 0.1 M lithium bis(trifluoromethanesulfonyl)imide salt in 1-ethyl-3-methylimidazolium tetrafluoroborate ionic liquid and dimethyl sulfoxide. Our results indicate that among the tested catalysts, ReS_2 exhibits the highest current density for both ORR and OER, beyond those of the state-of-the-art catalysts used in aprotic media with Li salts. We performed density functional calculations to provide a mechanistic understanding of the reactions in the ReS_2 NFs/ionic liquid system. These novel bifunctional catalyst results could open a way for exploiting the unique properties of these materials in Li−O_2 batteries as well as other important electrochemical systems.

INTRODUCTION

Transition metal dichalcogenides (TMDCs) have attracted worldwide research interest owing to their remarkable chemical, thermal, and electronic properties.[1,2] TMDCs have also shown interesting electrochemical properties, which make them promising candidates for energy conversion and storage applications. For instance, some TMDCs such as MoS_2 and WS_2 have been used as catalysts for CO_2 reduction,[3−6] hydrogen evolution reaction (HER),[7,8] oxygen reduction reaction (ORR), and oxygen evolution reaction (OER).[9,10] In particular, ORR and OER in electrolytes containing alkali salts are of great importance for energy storage as the specific energy and rechargeability of metal−O_2 batteries are governed by the rates of these reactions at the cathode and their corresponding overpotentials.[11] Of the metal−O_2 battery chemistries, the Li−O_2 system is the most well studied and has the highest theoretical energy density.

Despite the high theoretical energy density of Li−O_2 batteries, their low rate capability, poor cyclability, and low round-trip efficiency have impeded their development. These drawbacks originate from the sluggish kinetics of ORR and OER.[12] Hence, finding highly active bifunctional materials that can increase ORR and OER rates is crucial. To date, various catalytic materials such as carbon allotropes[13,14] and their composites,[15] noble metals,[16] and metal oxides[17,18] have been investigated for Li−O_2 systems. However, all of these materials are inefficient in practice; either they show low activity for

Received: October 8, 2019
Revised: March 16, 2020
Published: March 19, 2020

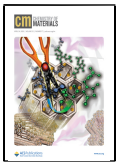

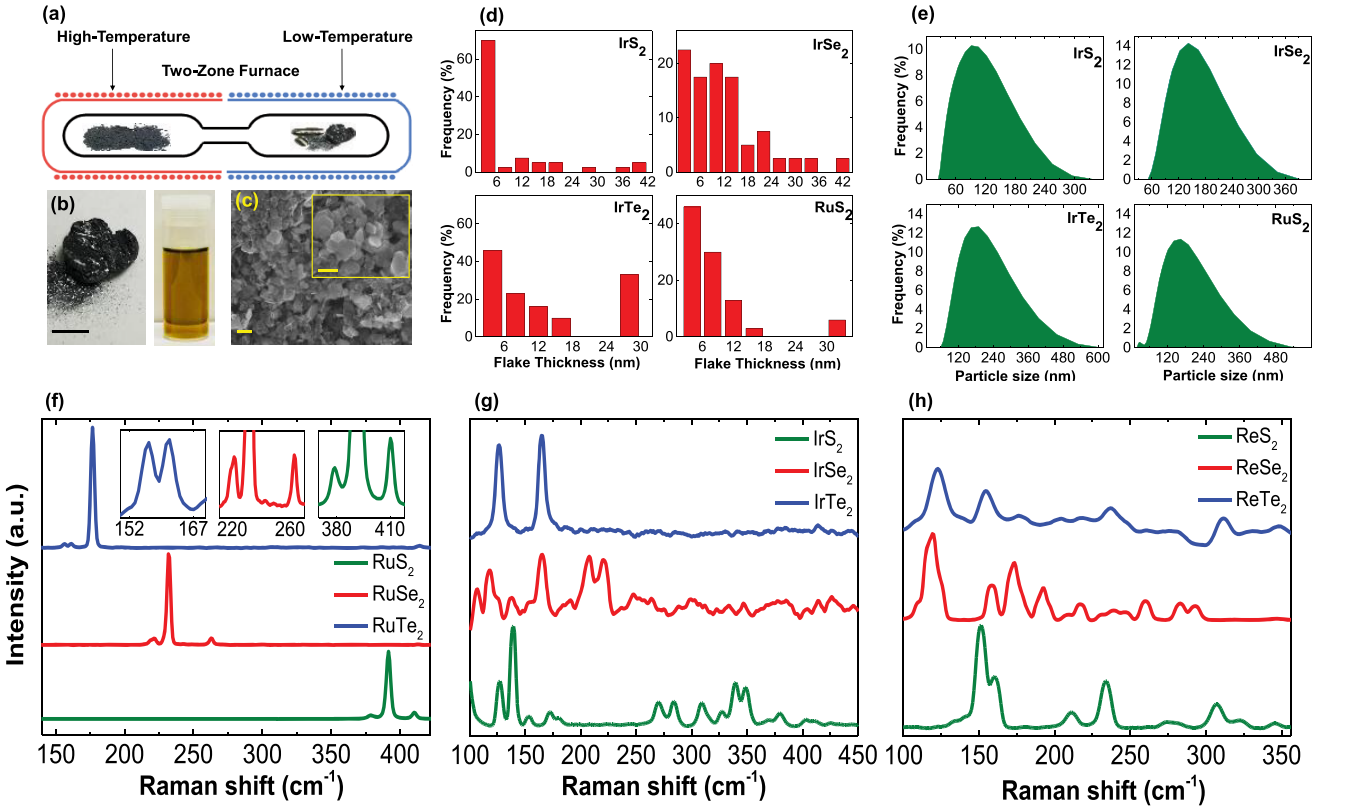

Figure 1. TMDC synthesis and characterization. (a) Schematic of the two-zone furnace for the chemical vapor transport method. (b) Representative photograph of (left) a bulk and (right) an exfoliated TMDC. Scale bar is 0.5 cm. (c) SEM images of deposited TMDC NFs on GDL. Scale bar is 100 nm. (d) Thickness distributions of TMDC NFs obtained with atomic force microscopy measurements. (e) Dynamic light scattering results for TMDC NFs lateral size distributions. (f–h) Raman scattering spectra obtained for as-synthesized materials.

ORR and/or OER or they exhibit poor stability upon the long-term cycling. Our recent work showed that TMDCs including sulfides, selenides, and tellurides of group V and VI transition metals exhibit outstanding catalytic performance for both ORR and OER in an aprotic medium with Li salts.[9,10,19] Motivated by this finding and to broaden the collection of highly efficient electrocatalysts for ORR/OER, we explore the synthesis, characterization, and catalytic performance of less studied TMDCs based on three transition metals, rhenium, ruthenium, and iridium, and three chalcogens, sulfur, selenium, and tellurium. Previously, rhenium-based TMDCs such as rhenium disulfide (ReS_2) and rhenium diselenide ($ReSe_2$) have shown promising behavior in lithium-ion[20] batteries and interesting catalytic characteristics for hydrogen evolution reaction (HER)[21−27] and lithium sulfur[25] batteries. Moreover, ruthenium and iridium in the form of metals and oxides have shown significant catalytic activity toward OER[28−30] and ORR.[31] However, only a few studies have focused on the role of ruthenium and iridium accompanied by the heavier chalcogens in electrochemical systems.[32−35]

RESULTS AND DISCUSSION

The studied TMDCs were synthesized by the chemical vapor transport (CVT) method[3] in which the transition metals and chalcogen powders were mixed in their stoichiometric ratios and placed in sealed quartz ampules. The ampules were then loaded in a two-zone furnace for the crystal growth process (Figure 1a). Section S1 of the Supporting Information describes further the details of the material synthesis process. To prepare the nanoflakes (NFs) of TMDCs, the as-prepared powders were exfoliated in isopropyl alcohol (IPA) with high-energy probe sonication followed by a centrifugation process (Figure 1b). A typical scanning electron microscopy (SEM) image of the synthesized materials coated on a gas diffusions layer (GDL) is presented in Figure 1c, and a higher magnification image is shown in the inset of Figure 1c. The images show that the flakes are packed together and positioned randomly. Atomic force microscopy (AFM) was employed to determine the thickness distributions of the exfoliated materials. Figure 1d represents the histogram of the flake thickness distributions of IrS_2, $IrSe_2$, $IrTe_2$, and RuS_2 in IPA obtained from the height profiles of 30−40 random individual flakes for each material. The thickness of the flakes ranged from 2 to 40 nm. Moreover, the lateral size of the synthesized materials was measured by dynamic light scattering (DLS) experiments. The average of the lateral size of these particles varies in the range from 116 to 230 nm as shown in Figure 1e. The AFM images obtained for a selected number of synthesized TMDCs are shown in the Supporting Information section S2.

Raman spectroscopy was performed to confirm the successful synthesis of all CVT-grown TMDC powders. A laser excitation wavelength of 785 nm was used for all Raman measurements. The Raman spectra of the ruthenium-containing TMDCs are shown in Figure 1f. $RuTe_2$ Raman peaks are located at 156.3, 161.1, and 176.9 cm^{-1} where the first and last peaks are attributed to E_g and A_g modes.[36] The Raman spectrum of $RuSe_2$ indicates three distinct peaks at 221.3, 232.01, and 263.2 cm^{-1}. The first and second peaks are attributed to E_g and A_g vibrational modes.[37,38] RuS_2 main

https://dx.doi.org/10.1021/acs.chemmater.9b04117
Chem. Mater. 2020, 32, 2764−2773

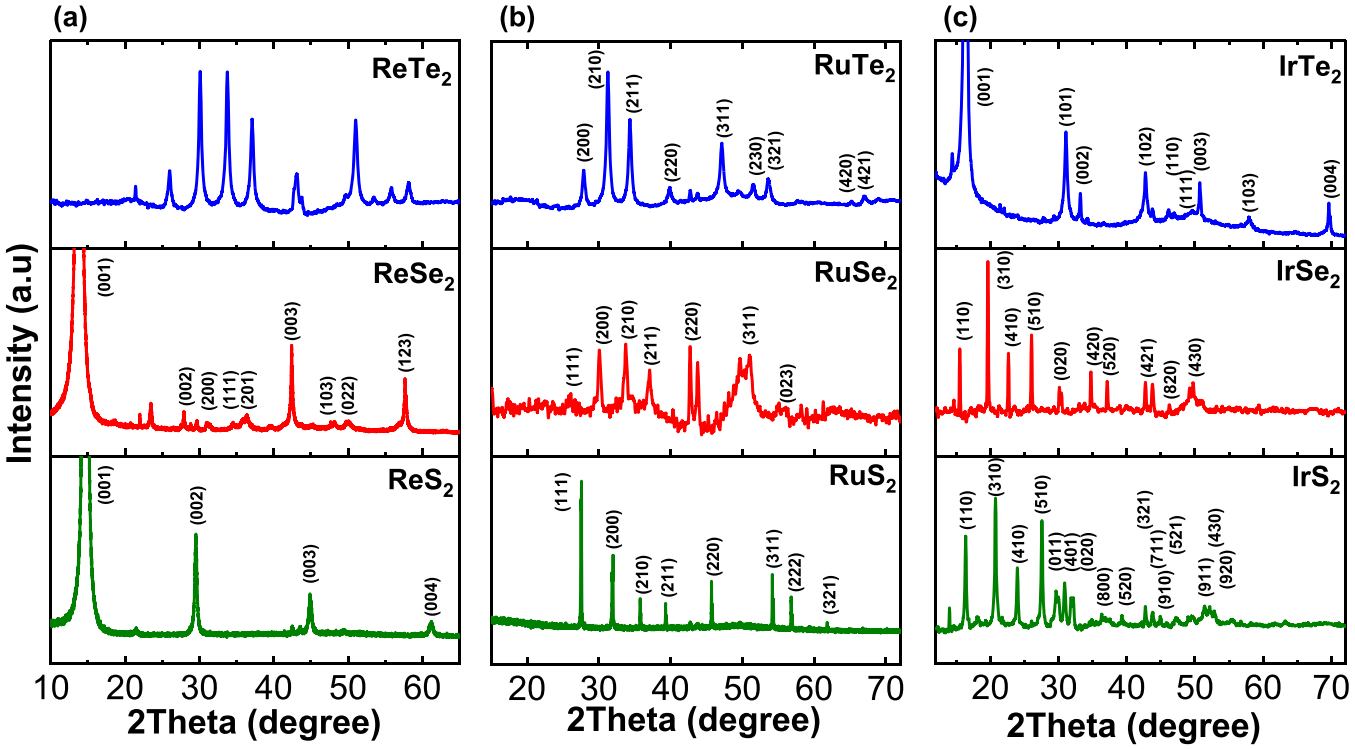

Figure 2. X-ray diffraction spectroscopy. (a) Rhenium-, (b) ruthenium-, and (c) iridium-based TMDCs. XRD patterns were matched with ReS_2 (ICDD card 00-052-0818), $ReSe_2$ (PDF card 00-052-0828), RuS_2 (ICDD card 01-080-0669), $RuSe_2$ (ICDD card 03-065-3328), $RuTe_2$ (ICDD card 00-019-1108), IrS_2 (ICDD card -00-046-1207 IrS_2), $IrSe_2$ (ICDD card 01-085-0486), and $IrTe_2$ (ICDD card 01-076-0411). Diffraction pattern is truncated at the (001) reflection for ReS_2, $ReSe_2$, and $IrTe_2$ to show all of the peaks. ICDD and PDF stand for International Centre for Diffraction Data and Powder Diffraction File, respectively.

peaks were located at 378.9, 391.8, and 410.1 cm^{-1}. The first two peaks of RuS_2 belong to the E_g or T_g mode, and the 410.1 cm^{-1} peak corresponds to the A_g mode.[39] In Figure 1g, the Raman spectra of iridium-based TMDCs are shown. IrS_2 and $IrSe_2$ show numerous Raman peaks in the selected range. IrS_2 distinct Raman peaks were observed at 100.7, 127.5, 139.9, 153.09, 171.7, 180.44, 269.8, 283.9, 309, 237.2, 339.08, 349.1, 369.2, 379.26, 402.9, 410.2, and 425.29 cm^{-1}. The main Raman peaks for $IrSe_2$ appeared at 106.1, 118.04, 137.2, 153.09, 165.44, 186.4, 190, 207.3, 220.14, 236.5, 247.4, 264.8, 274.8, 288.5, and 298.5 cm^{-1}. The positions of the peaks are in good agreement with previously reported Raman spectra of IrS_2 and $IrSe_2$.[40] The main iridium telluride ($IrTe_2$) Raman peaks were observed at 126.4 and 164.9 cm^{-1}, which correspond to E_{2g} and A_{1g} vibrational modes.[41] Figure 1h shows the Raman spectra of ReS_2, $ReSe_2$, and $ReTe_2$. The distinctive Raman peaks of ReS_2 appeared at 151.5, 160.5, 211.2, 234.2, and 307.04 cm^{-1}, where the peaks at 160.5 and 211.2 cm^{-1} correspond to in-plane E_g and out-of-plane A_g vibrational modes, respectively.[42,43] $ReSe_2$ has two characteristic vibrational modes observed at 123.48 and 157.96 cm^{-1}, where the first one is an E_g-like mode and the latter is an A_g-like mode.[43,44] Distinct Raman peaks of $ReTe_2$ were located at 122.8, 154.5, 236.91, and 311.2 cm^{-1}.

The X-ray diffraction (XRD) experiment was performed on the synthesized TMDCs (Figure 2). The TMDC NFs were drop cast on a silicon wafer for this purpose. The strong peaks recorded for all patterns suggest that the materials are highly crystalline. The recorded XRD data were matched and indexed with patterns for the pure compounds extracted from the powder diffraction database by the International Centre for Diffraction Data (ICDD). The patterns generally showed a good match to the theoretical reflections as well as data in the literature and no evidence of impurity phases, with the exception of an unidentified peak at 24°, 2θ, for $ReSe_2$.[45−52] The pattern of $ReTe_2$ deviated from the crystallographic data for the polymorphs reported in the literature,[53−55] but no obvious signs of impurities, such as the initial elemental reagents and their respective oxides, were found.[56−59] It is possible that a new polymorph of $ReTe_2$ was made in these conditions.[53] This possibility will be further explored in follow-up reports. The diffraction pattern of ReS_2 only showed (00l) reflections, implying the exfoliated particles were preferentially oriented along the c axis. The XRD results of ReS_2 NFs coated on GDL are also presented in section S4 of the Supporting Information as representative of the actual cathode used in the electrochemical experiments.

Furthermore, the chemical states and composition of synthesized TMDCs were verified using X-ray photoelectron spectroscopy (XPS) experiments. Section S5 of the Supporting Information shows the XPS results of synthesized MX_2 NFs (M = Re, Ru, and Ir and X = S, Se, and Te).

To investigate the electrochemical performance of the synthesized catalysts for ORR and OER, a standard three-electrode electrochemical cell was used (see section S6 of the Supporting Information). Cyclic voltammetry (CV) experiments were carried out in an O_2-saturated electrolyte including 0.1 M lithium bis(trifluoromethanesulfonyl)imide (LiTFSI) dissolved in 1-ethyl-3-methylimidazolium tetrafluoroborate (EMIM−BF_4) ionic liquid and dimethyl sulfoxide (DMSO) with an optimized 1:3 volumetric ratio.[10] The current density results were recorded by a sweeping potential with a scan rate

https://dx.doi.org/10.1021/acs.chemmater.9b04117
Chem. Mater. 2020, 32, 2764−2773

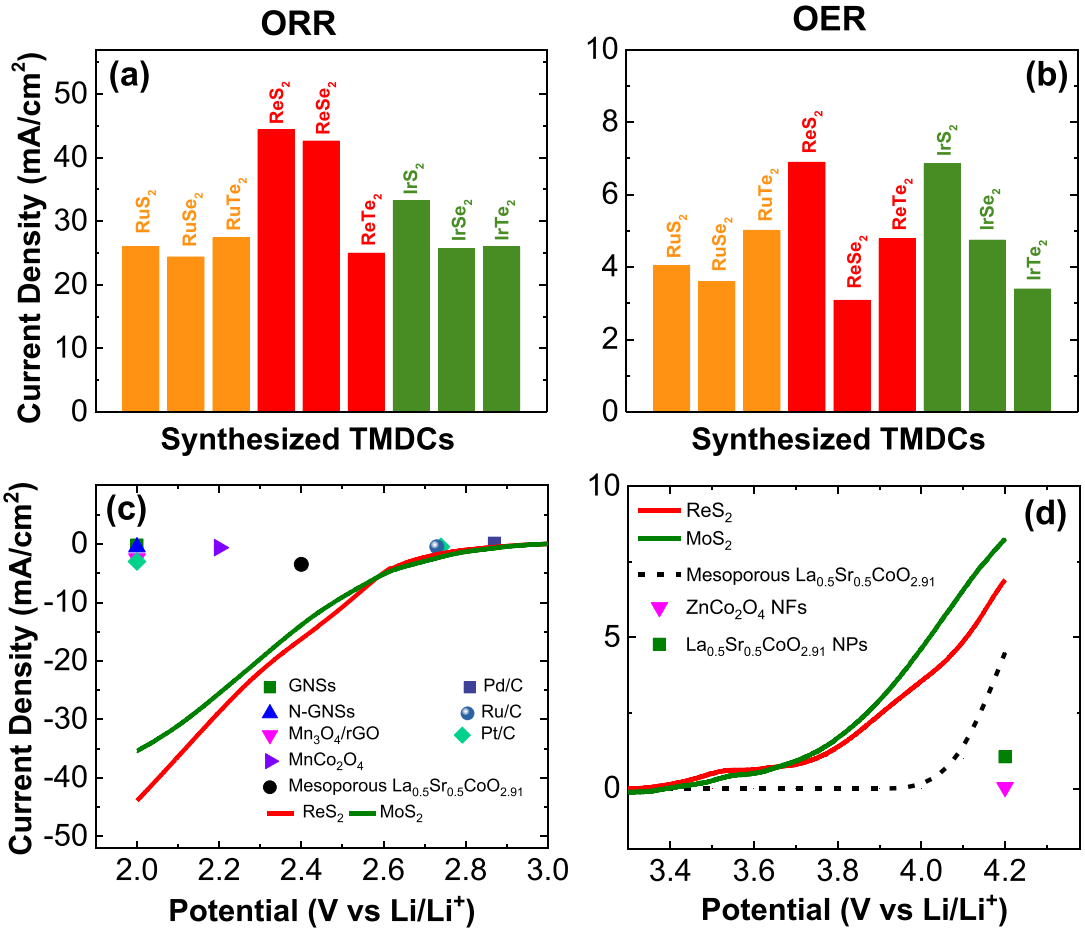

Figure 3. Comparison of ORR−OER activity of synthesized TMDCs. Current density results of CV experiments in O_2-saturated IL, DMSO, and lithium bis(trifluoromethanesulfonyl)imide salt with a scan rate of 20 mV/s for (a) ORR, (b) OER, and (c and d) ORR and OER current densities of ReS_2, MoS_2, and reported catalysts in aprotic media with Li salts.[16,50−56]

of 20 mV/s in the potential window from 2.0 to 4.2 V vs Li/Li$^+$. For cathode preparation, the GDL substrates were coated with each of the synthesized TMDC NFs. We used GDLs in three-electrode cell experiments to mimic the real conditions occurring in the Li−O_2 battery assemblies.[9,10,19] The CV profiles of the synthesized TMDC NFs are presented in the Supporting Information section S6. The obtained current densities at the ORR and OER cutoff potentials are presented in Figure 3a and 3b for each family of synthesized TMDCs. The reported current densities are normalized based on the geometric surface area of the electrode. Among the nine different TMDCs and at a potential of 2.0 V, ReS_2 demonstrates the highest current density of 44.37 mA/cm^2 for ORR (Figure 3a). $ReSe_2$ shows the second highest ORR current density of 42.61 mA/cm^2. At a potential of 4.20 V and at the end of OER, the ReS_2 catalyst also exhibits the highest current density of 6.89 mA/cm^2 (Figure 3b). The IrS_2 has an OER activity similar to ReS_2 (current density of 6.85 mA/cm^2). According to the results of the CV experiments, ReS_2 was found to be the best catalyst among the nine TMDCs, showing a significantly higher catalytic activity for both ORR and OER.

Figure 3c and 3d shows the CV results for the ReS_2 catalyst during ORR and OER in comparison with our previously obtained results for MoS_2[19] and the reported state-of-the-art catalysts in aprotic media with Li salts, including noble metals (e.g., Au, Pt),[16,60,61] metal oxides (e.g., Mn_3O_4),[62,63] perovskite (e.g., $La_{0.5}Sr_{0.5}CoO_{2.91}$),[64] and doped carbon nanomaterials (e.g., N-doped graphene).[65] This comparison shows that during ORR, at a potential of 2.00 V vs Li/Li$^+$, the current density of ReS_2 catalyst reaches 44.37 mA/cm^2, which is more than 14 times higher than current densities achieved by noble metals or oxide catalysts.[62] Moreover, the obtained ORR current density at 2.00 V vs Li/Li$^+$ is considerably higher than that of MoS_2 NFs (35.4 mA/cm^2), which has been reported as a highly active TDMC catalyst for ORR.[19]

As shown in Figure 3d, the OER current density of ReS_2 reaches 6.89 mA/cm^2 at a potential of 4.20 V. This exceeds the current density of mesoporous $ZnCo_2O_4$ NFs,[66] $La_{0.5}Sr_{0.5}CoO_{2.91}$ nanoparticles (NPs),[64] and mesoporous $La_{0.5}Sr_{0.5}CoO_{2.91}$ at the same potential.[64] We note that the OER onset potential of ReS_2 (approximately 3.40 V) is much lower than that of $La_{0.5}Sr_{0.5}CoO_{2.91}$ (approximately 4.0 V), as shown in Figure 3d. Compared to MoS_2, which has a current density of 8.26 mA/cm^2 at 4.2 V vs Li/Li$^+$,[19] the ReS_2 catalyst shows slightly less OER activity.

To examine the chemical stability of the ReS_2 catalyst, we performed XPS after 10 h of chronoamperometry experiment at 2.7 V vs Li/Li$^+$. The XPS spectra are shown in section S7 of the Supporting Information. Our results indicate that the ReS_2 characteristic peak intensities and positions do not change after the long-term experiment. A new peak with a very low intensity was also observed in the sulfur region at a binding energy of

https://dx.doi.org/10.1021/acs.chemmater.9b04117
Chem. Mater. 2020, 32, 2764−2773

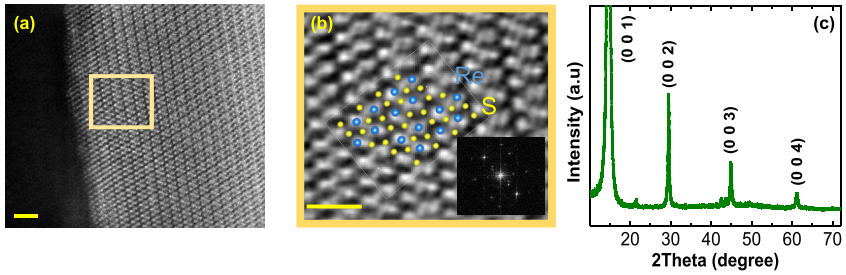

Figure 4. Crystal structure of synthesized ReS_2 NFs. (a) Atomic resolution TEM images of a ReS_2 NF. Scale bar is 2 nm. (b) Magnified TEM image of the selected area (scale bar is 0.5 nm). FFT pattern is also indicated in the inset. (c) XRD results of ReS_2 NFs deposited on silicon substrate. XRD pattern was matched with ReS_2 (ICDD card 00-052-0818).[45]

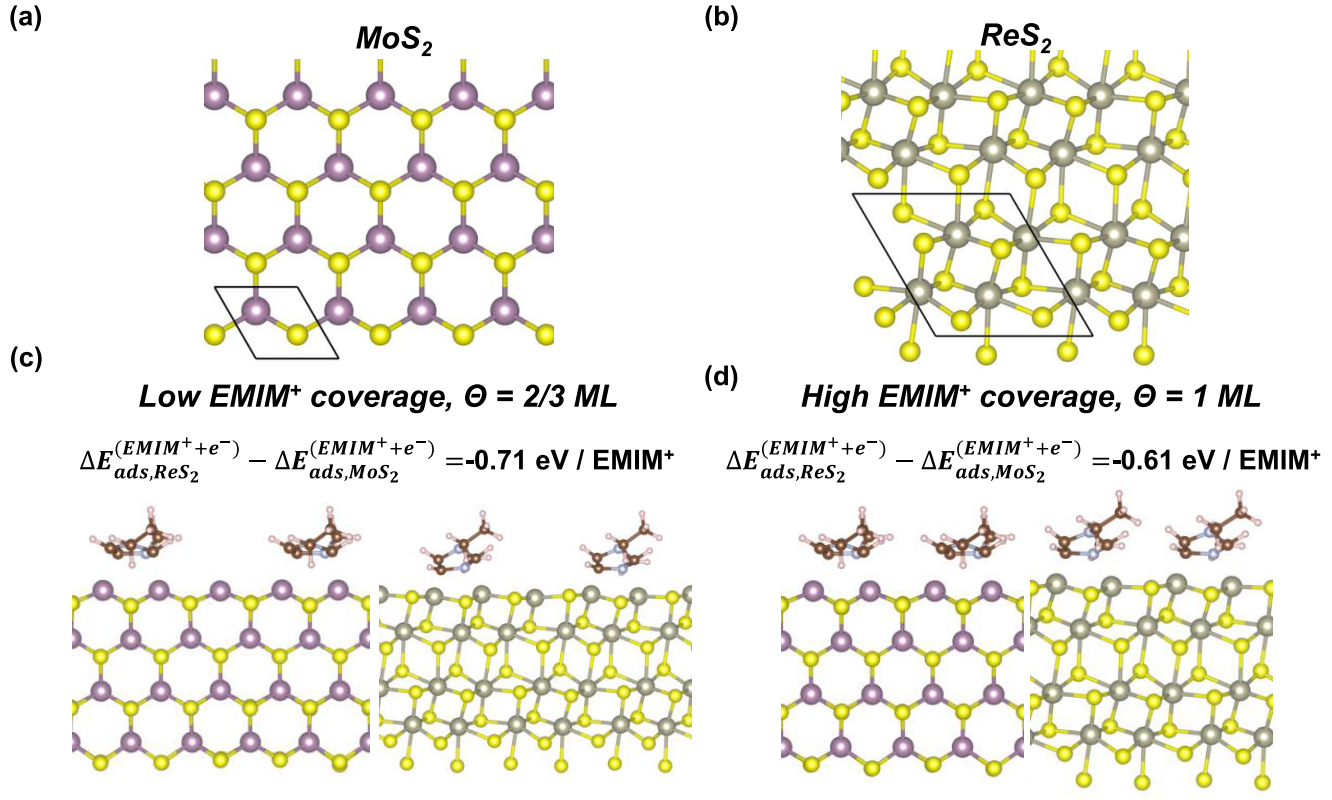

Figure 5. Calculated bulk structures and ionic liquid adsorption on MoS_2 and ReS_2 edges. Bulk structures from DFT calculations on (a) MoS_2 and (b) ReS_2. Black boxes indicate the primitive bulk unit cell viewed in the [001] direction, where the ReS_2 primitive cell is defined by more atoms due to symmetry lowering caused by formation of Re dimer-like configurations in the lattice. (c) Adsorption of ($EMIM^+ + e^-$) pairs on metal-terminated MoS_2 and ReS_2 catalyst edges, where 2/3 of the metal sites are covered by the $EMIM^+$ cations, exposing isolated metal sites. (d) Adsorption of ($EMIM^+ + e^-$) pairs on MoS_2 and ReS_2 where all metal sites are covered by $EMIM^+$ cations, likely to be more relevant at low voltages (or high ORR overpotentials).

168.9 eV, which matches with the binding energy of sulfur in a sulfate group.[67]

In this study, the ReS_2 NFs were further characterized using high-resolution scanning transmission electron microscopy (STEM) to identify the structure of ReS_2 NFs, which is then used to create realistic atomic configurations for our density functional theory (DFT) calculations. Low-magnification TEM images obtained for a selected number of TMDCs are also presented in section S2 of the Supporting Information. Figure 4a shows the atomic resolution high-angle annular dark-field (HAADF) image from the edge of the ReS_2 nanosheet in the [001] zone axis, where Re atomic columns are clearly resolved. Figure 4b shows a magnified image from the selected area as well as a Fourier transformation (FFT) of the image shown as an inset. The spots in the FFT image showing hexagonal symmetry are indexed according to the distorted T phase (T′) of ReS_2 in the [001] zone axis orientation (see Figure S4(d)). The patterns match the XRD pattern shown in Figure 4c as well as the calculated structural model of ReS_2 in the [001] zone direction (see Figure 5). X-ray energy-dispersive spectroscopy (XEDS) and mapping data acquired from the selected area in Figure 4a further confirm the atomic ratio for Re and S elements in the ReS_2 sample (see section S3 of the Supporting Information).

To further understand the enhanced ORR rates for ReS_2 in comparison to MoS_2, we performed DFT calculations (see Supporting Information section S8). Previously, we used constrained DFT (CDFT) to shed light on the role of electron transfer in the ORR and OER on MoS_2 cathodes in ionic liquid and its relationship to catalytic activity.[19] We found that the

https://dx.doi.org/10.1021/acs.chemmater.9b04117
Chem. Mater. 2020, 32, 2764−2773

OER proceeds via diabatic charge transfer from the Li_2O_2 charge product, whereas ORR proceeds via adiabatic charge transfer, which helped to explain why OER rates are considerably lower than ORR rates for MoS_2 and the other TMDC materials studied in ref 19. These calculations could help to explain OER and ORR activities for ReS_2 by comparing the results with MoS_2. Since the OER rate for the ReS_2 catalyst is similar to that of MoS_2,[19] it presumably has a similar diabatic electron transfer mechanism and helps to explain its lower activity than ORR. It also suggests that ORR will have adiabatic charge transfer similar to MoS_2, which can account for the high ORR activity of ReS_2. We also note that the catalytically active sites required to reduce O_2 are on edge sites as described in work from our groups[3,9,10] as well as others in studies of electrocatalytic CO_2 reduction[68] and hydrogen evolution reactions.[69,70] Following charge transfer from the TMDC catalyst to reduce O_2, O_2^- anions react with Li^+ ions in solution to form LiO_2 monomers that gradually undergo a disproportionation-based nucleation and growth mechanism to form the Li_2O_2 discharge product as described in our previous work.[9]

Figure 5a and 5b shows the theoretical models for a single layer of two-dimensional MoS_2 and ReS_2 for DFT calculations. While each material adopts a similar bulk structure, our high-resolution STEM results (Figure 4b) show that there is a Peierls distortion for the ReS_2 lattice that reduces the bulk symmetry which was also shown in a recent computational study.[71] This effect leads to Re-ion dimerization in comparison to the presence of six equivalent Mo−Mo nearest neighbor distances in 2H MoS_2. As shown in previous work, cationic $EMIM^+$ ionic liquid components tend to migrate to cathode surfaces.[19,72,73] On MoS_2, ($EMIM^+ + e^-$) pairs bind strongly as suggested by the low energy of $EMIM^+$ states interacting with the MoS_2 edge in the electronic density of states.[9] On MoS_2, O_2 is reduced upon binding to edge Mo ions, while the edge is protected from oxidation by O_2 dissociation due to the presence of strongly bound $EMIM^+$ ions. Given the cocatalytic nature of the MoS_2/$EMIM^+$ that leads to high ORR rates on MoS_2, we also consider ($EMIM^+ + e^-$) pair binding to the edge of ReS_2. Figure 5c shows the structures of ($EMIM^+ + e^-$) pairs bound to the edges of MoS_2 and ReS_2 where two-thirds of metal ions on the edge are covered by the cationic ionic liquid fragments, exposing isolated metal sites that are catalytically active for O_2 reduction.[9] Not only do the ($EMIM^+ + e^-$) pairs bind to the ReS_2 edge despite the aforementioned bulk distortions of Re ions but also the results further suggest that the binding is significantly more exothermic (by 0.71 eV per $EMIM^+$) in comparison to MoS_2.

We note that since the reaction of an ($EMIM^+ + e^-$) pair with the catalyst edge involves a charged species and electron transfer, the absolute binding energy is always dependent on the electrochemical potential.[57] More specifically, cation binding energies become more favorable for lower potentials (or higher ORR overpotentials) as the electrode prefers to adopt a more negative charge due to shifting of the Fermi level to higher energies. To further probe these differences between ReS_2 and MoS_2, we performed DFT calculations considering a higher coverage of the ionic liquid. Figure 5d shows ($EMIM^+ + e^-$) pairs binding at full coverage, where all metal ions are covered by the $EMIM^+$ cations. The results show that at higher coverage ($EMIM^+ + e^-$) pairs still bind more strongly to ReS_2 in comparison to MoS_2 (by 0.61 eV per $EMIM^+$). This suggests that there is an enhanced driving force for full coverage of $EMIM^+$ ions on the edge of ReS_2 at low potentials under ORR conditions.

The full coverage of edge Re ions by $EMIM^+$ ions at low voltage has implications for ORR catalysis, since the availability of metal ions at the TMDC edge are necessary for oxygen reduction to occur. Despite the stronger binding and thus higher coverage of $EMIM^+$ ions to the ReS_2 edge, it maintains a higher activity than MoS_2[19] at higher potentials (see Figure 3c). In order to explain the reactivity of ReS_2 catalysts, we assess whether O_2 reduction may still be feasible in the limit of full $EMIM^+$ coverage on both the MoS_2 and the ReS_2 catalysts. Figure 6 shows the adsorption of O_2 of MoS_2 and ReS_2 edges

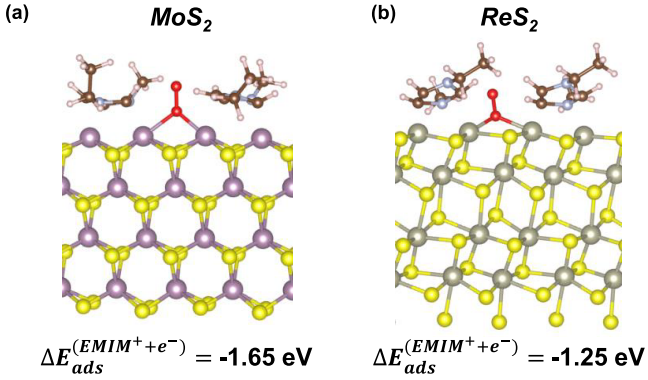

Figure 6. Oxygen adsorption and reduction on TDMC edges in the high $EMIM^+$ coverage limit. DFT-calculated structures and adsorption energies for O_2 adsorption on (a) MoS_2 and (b) ReS_2 with $EMIM^+$ coverage of Θ = 1 ML in an upright configuration with one oxygen atom forming bonds between two metal ions.

with full coverage of $EMIM^+$ cations, where O_2 binding is exothermic in each case (by 1.65 and 1.25 eV for MoS_2 and ReS_2, respectively). This suggests that O_2 reduction could occur despite full coverage of metal-ion edge sites by ionic liquid. Moreover, while O_2 binding is exothermic in the limit of high $EMIM^+$ coverage for both catalysts, the stronger binding to MoS_2 may suggest slower desorption following O_2 reduction, as suggested by higher ORR activities for ReS_2 in comparison to MoS_2. Given that O_2 may adsorb on metal top sites or bridge sites for coverages of Θ = 2/3 or 1 ML, respectively, this corresponds to one active site per adsorbed $EMIM^+$ ion. Considering this within the context of the stronger relative binding energies of $EMIM^+$ ions on ReS_2, we speculate that more metal ions may be active for ORR per edge length on ReS_2 in comparison to MoS_2 as the ORR overpotential is increased.

CONCLUSIONS

In summary, a new family of TMDCs was successfully synthesized based on rhenium, ruthenium, and iridium through the CVT method. Various characterization methods such as DLS, Raman spectroscopy, XPS, STEM, and XRD were performed for the bulk and exfoliated NFs of these materials. The catalytic activity of these catalysts was examined for ORR and OER reactions in the aprotic electrolyte (DMSO/IL) with lithium LiTFSI salt. Although excellent performance was observed in both ORR and OER for all of the prepared catalysts, ReS_2 showed the highest current densities of 44.37 mA/cm^2 during ORR and 6.89 mA/cm^2 during OER. DFT calculations show that in the presence of $EMIM^+$ cations, binding of O_2 to the catalytic TMDC edges is still highly

https://dx.doi.org/10.1021/acs.chemmater.9b04117
Chem. Mater. 2020, 32, 2764−2773

favorable for both ReS_2 and MoS_2, which explains their high ORR activities. DFT calculations suggest that, in comparison to MoS_2, stronger binding of $EMIM^+$ cations to ReS_2 may increase the density of active metal ions on the catalyst edge that participate in ORR under the reaction conditions. The dynamic nature of the voltage-dependent coverage of ionic liquid cationic fragments highlights the cocatalytic effects between the TMDCs and the electrolyte. The bifunctional ORR and OER rate capabilities exhibited by TMDCs in ionic liquid present opportunities for implementing 2D electrocatalytic materials for various energy conversion and storage applications, such as metal−O_2 batteries.

EXPERIMENTAL PROCEDURES

Materials Synthesis. One gram of transition metal and chalcogen powders with a 1:2 stoichiometric ratio was mixed and loaded in an evacuated and sealed quartz ampule. The ampule was then placed in a two-zone furnace. During 24 h, the temperature of both zones was raised to 1080 °C. The temperature of the cold zone gradually decreased to 950 °C in 4 days, while the temperature of the hot zone was maintained at 1080 °C. The furnace was cooled down to room temperature in 24 h. The NFs of TMDCs were obtained using a liquid exfoliation method via a 30 h ultrasonication process (Vibra Cell Sonics 130 W) on the synthesized TMDC powders disrpersed in IPA followed by centrifugation.

Raman Specroscopy. The Raman spectroscopy was performed using a Horiba LabRAM HR Evolution confocal Raman microscope with a 785 nm laser wavelength and 50x objective using a Horiba Andor detector.

X-ray Diffraction (XRD). The samples were prepared through drop casting of TMDC NFs on silicon substrates. Powder XRD was performed for all of the nine TMDC NFs on a Bruker D8 Advance (40 kV, 40 mA) using a Cu Kα (λ_{avg} = 1.5418 Å). The diffraction pattern was recorded from 10° to 70° (2θ).

X-ray Photoelectron Spectroscopy (XPS). A Thermo Scientific ESCALAB 250Xi instrument was utilized to carry out XPS experiments. A calibration was performed in all of the obtained spectra based on the peak position of the C−C bond located at 284.8 eV. Thermo Avantage software was used to anaylze and process the data.

Atomic Forced Microscopy (AFM). A Bruker ICON Dimension was used to obtain the topography maps of drop-cast flakes and the statistical flake thickness distributions. Exfoliated TMDC dispersions in IPA were drop cast on silicon substrates. The substrates were carefully washed by acetone, IPA, and deionazied water. They were evantually annealed under a temperature of 120 °C for 1 h.

Dynamic Light-Scattering Measurement (DLS). Measurements of the lateral size of the flakes were performed using the Malvern Zetasizer Nano ZSP system at 25 °C. A 10 mW semiconductor laser with 633 nm emission is used in this instrument.

Transmission Electron Microscopy (TEM). The TEM experiments were performed using the aberration-corrected JEOL JEM-ARM200CF STEM operating at an acceleration voltage of 200 kV. The high-angle annular dark-field (HAADF) images were acquired using a convergence semiangle of 23 mrad and a collection angle from 90 to 175 mrad. The atomic resolution images were recorded using pixel dwell time of 31 μs. The chemical composition of the ReS_2 sample is obtained via XEDS using a windowless silicon drift detector X-Max^N 100TLE.

Electrochemical Experiments. A standard three-electrode cell was used to evaluate the catalytic activity of the synthesized TMDCs (Supporting Information S6). To prepare the working electrodes, TMDC NFs were coated on GDL with a loading of 0.1 mg/cm^2 (Sigracet 25 BC, purchased from FuelCellsEtc).

ASSOCIATED CONTENT

Supporting Information

The Supporting Information is available free of charge at https://pubs.acs.org/doi/10.1021/acs.chemmater.9b04117.

Materials synthesis details, AFM and TEM images, ReS_2 EDX results, XRD results of bare and coated GDL, TMDC XPS results, CV profiles of TMDCs, ReS_2 stability test results, and additional details on DFT calculations (PDF)

AUTHOR INFORMATION

Corresponding Authors

Larry A. Curtiss − *Materials Science Division, Argonne National Laboratory, Argonne, Illinois 60439, United States;* orcid.org/0000-0001-8855-8006; Email: curtiss@anl.gov

Amin Salehi-Khojin − *Department of Mechanical and Industrial Engineering, University of Illinois at Chicago, Chicago, Illinois 60607, United States*; Email: salehikh@uic.edu

Authors

Leily Majidi − *Department of Mechanical and Industrial Engineering, University of Illinois at Chicago, Chicago, Illinois 60607, United States;* orcid.org/0000-0002-8058-5648

Zahra Hemmat − *Department of Mechanical and Industrial Engineering, University of Illinois at Chicago, Chicago, Illinois 60607, United States;* orcid.org/0000-0002-6463-8404

Robert E. Warburton − *Davidson School of Chemical Engineering, Purdue University, West Lafayette, Indiana 47907, United States*

Khagesh Kumar − *Department of Chemistry, University of Illinois at Chicago, Chicago, Illinois 60607, United States*

Alireza Ahmadiparidari − *Department of Mechanical and Industrial Engineering, University of Illinois at Chicago, Chicago, Illinois 60607, United States*

Liang Hong − *Department of Physics, University of Illinois at Chicago, Chicago, Illinois 60607, United States;* orcid.org/0000-0003-1499-5806

Jinglong Guo − *Department of Physics, University of Illinois at Chicago, Chicago, Illinois 60607, United States*

Peter Zapol − *Materials Science Division, Argonne National Laboratory, Argonne, Illinois 60439, United States;* orcid.org/0000-0003-0570-9169

Robert F. Klie − *Department of Physics, University of Illinois at Chicago, Chicago, Illinois 60607, United States*

Jordi Cabana − *Department of Chemistry, University of Illinois at Chicago, Chicago, Illinois 60607, United States;* orcid.org/0000-0002-2353-5986

Jeffrey Greeley − *Davidson School of Chemical Engineering, Purdue University, West Lafayette, Indiana 47907, United States;* orcid.org/0000-0001-8469-1715

Complete contact information is available at: https://pubs.acs.org/10.1021/acs.chemmater.9b04117

Author Contributions

L.M. synthesized the TMDCs bulk and NFs and performed the electrochemical experiments. L.M. and Z.H. carried out Raman experiments. Z.H. obtained the SEM images. K.K, J.C., and L.M. performed XRD experiments and analysis. L.M. performed XPS. L.M. and A.A. performed AFM and DLS. A.S.K. supervised the characterization and electrochemical experiments. R.E.W., P.Z., J. G., and L.A.C. carried out the

https://dx.doi.org/10.1021/acs.chemmater.9b04117
Chem. Mater. 2020, 32, 2764−2773

computational studies (DFT) of ReS_2/IL systems. L.H., J.G., and R.F.K. performed STEM and EELS experiments. All of the authors contributed to the manuscript before submission.

Notes

The authors declare no competing financial interest.

■ ACKNOWLEDGMENTS

The work of A.S.K., R.F.K., L.M., Z.H., L.H., J.G., and A.A. was supported by the National Science Foundation DMREF Grants 1729420 and CBET-1800357. L.H. and R.F.K. also acknowledge funding from the National Science Foundation (DMR-0959470 and DMR-1626065) for acquisition of the UIC JEOL JEMARM200CF with the Gatan Quantum GIF EELS spectrometer. Work by P.Z. and L.A.C. was supported by the US Department of Energy, BES Materials Sciences under Contract DEAC02-06CH11357 with UChicago Argonne, LLC, operator of Argonne National Laboratory. J.G.'s work was supported through a Department of Energy award through the Office of Science, Office of Basic Energy Sciences, Chemical, Biological, and Geosciences Division, under award number DE-SC0010379. K.K. and J.C. were supported by the National Science Foundation under grant no. CBET-1800357. R.E.W. acknowledges the U.S. Department of Energy, Office of Science, Office of Workforce Development for Teachers and Scientists, Office of Science Graduate Student Research (SCGSR) Program. The SCGSR program is administered by the Oak Ridge Institute for Science and Education (ORISE) for the DOE. ORISE is managed by ORAU under contract number DE-SC0014664. The authors thank Dr. Xinqi Chen at the Atomic and Nanoscale Characterization Experimental Center (NUANCE) in Northwestern University for insightful discussions and guidance.

■ REFERENCES

(1) Manzeli, S.; Ovchinnikov, D.; Pasquier, D.; Yazyev, O. V.; Kis, A. 2D Transition Metal Dichalcogenides. *Nat. Rev. Mater.* **2017**, *2*, 17033.

(2) Chhowalla, M.; Shin, H. S.; Eda, G.; Li, L.-J.; Loh, K. P.; Zhang, H. The Chemistry of Two-Dimensional Layered Transition Metal Dichalcogenide Nanosheets. *Nat. Chem.* **2013**, *5* (4), 263−275.

(3) Asadi, M.; Kim, K.; Liu, C.; Addepalli, A. V.; Abbasi, P.; Yasaei, P.; Phillips, P.; Behranginia, A.; Cerrato, J. M.; Haasch, R.; et al. Nanostructured Transition Metal Dichalcogenide Electrocatalysts for CO_2 Reduction in Ionic Liquid. *Science* **2016**, *353* (6298), 467−470.

(4) Abbasi, P.; Asadi, M.; Liu, C.; Sharifi-Asl, S.; Sayahpour, B.; Behranginia, A.; Zapol, P.; Shahbazian-Yassar, R.; Curtiss, L. A.; Salehi-Khojin, A. Tailoring the Edge Structure of Molybdenum Disulfide toward Electrocatalytic Reduction of Carbon Dioxide. *ACS Nano* **2017**, *11* (1), 453−460.

(5) Asadi, M.; Motevaselian, M. H.; Moradzadeh, A.; Majidi, L.; Esmaeilirad, M.; Sun, T. V.; Liu, C.; Bose, R.; Abbasi, P.; Zapol, P.; et al. Highly Efficient Solar-Driven Carbon Dioxide Reduction on Molybdenum Disulfide Catalyst Using Choline Chloride-Based Electrolyte. *Adv. Energy Mater.* **2019**, *9* (9), 1803536.

(6) Ahmadiparidari, A.; Warburton, R. E.; Majidi, L.; Asadi, M.; Chamaani, A.; Jokisaari, J. R.; Rastegar, S.; Hemmat, Z.; Sayahpour, B.; Assary, R. S.; et al. A Long-Cycle-Life Lithium-CO_2 Battery with Carbon Neutrality. *Adv. Mater.* **2019**, *31*, 1902518.

(7) Lukowski, M. A.; Daniel, A. S.; English, C. R.; Meng, F.; Forticaux, A.; Hamers, R. J.; Jin, S. Highly Active Hydrogen Evolution Catalysis from Metallic WS_2 Nanosheets. *Energy Environ. Sci.* **2014**, *7* (8), 2608−2613.

(8) Behranginia, A.; Asadi, M.; Liu, C.; Yasaei, P.; Kumar, B.; Phillips, P.; Foroozan, T.; Waranius, J. C.; Kim, K.; Abiade, J.; et al. Highly Efficient Hydrogen Evolution Reaction Using Crystalline Layered Three-Dimensional Molybdenum Disulfides Grown on Graphene Film. *Chem. Mater.* **2016**, *28* (2), 549−555.

(9) Asadi, M.; Kumar, B.; Liu, C.; Phillips, P.; Yasaei, P.; Behranginia, A.; Zapol, P.; Klie, R. F.; Curtiss, L. A.; Salehi-Khojin, A. Cathode Based on Molybdenum Disulfide Nanoflakes for Lithium-Oxygen Batteries. *ACS Nano* **2016**, *10* (2), 2167−2175.

(10) Asadi, M.; Sayahpour, B.; Abbasi, P.; Ngo, A. T.; Karis, K.; Jokisaari, J. R.; Liu, C.; Narayanan, B.; Gerard, M.; Yasaei, P.; et al. A Lithium-Oxygen Battery with a Long Cycle Life in an Air-like Atmosphere. *Nature* **2018**, *555* (7697), 502−506.

(11) Shao, Y.; Park, S.; Xiao, J.; Zhang, J.; Wang, Y.; Liu, J. Electrocatalysts for Nonaqueous Lithium-Air Batteries: Status, Challenges, and Perspective. *ACS Catal.* **2012**, *2* (5), 844−857.

(12) Surya, K.; Michael, M. S.; Prabaharan, S. R. S. A Review on Advancement in Non-Noble Metal Based Oxides as Bifunctional Catalysts for Rechargeable Non-Aqueous Li/Air Battery. *Solid State Ionics* **2018**, *317*, 89−96.

(13) Li, Y.; Wang, J.; Li, X.; Liu, J.; Geng, D.; Yang, J.; Li, R.; Sun, X. Nitrogen-Doped Carbon Nanotubes as Cathode for Lithium-Air Batteries. *Electrochem. Commun.* **2011**, *13* (7), 668−672.

(14) Ren, X.; Zhang, S. S.; Tran, D. T.; Read, J. Oxygen Reduction Reaction Catalyst on Lithium/Air Battery Discharge Performance. *J. Mater. Chem.* **2011**, *21* (27), 10118.

(15) Shui, J. L.; Karan, N. K.; Balasubramanian, M.; Li, S. Y.; Liu, D. J. Fe/N/C Composite in Li-O_2 Battery: Studies of Catalytic Structure and Activity toward Oxygen Evolution Reaction. *J. Am. Chem. Soc.* **2012**, *134* (40), 16654−16661.

(16) Lu, Y. C.; Gasteiger, H. A.; Shao-Horn, Y. Catalytic Activity Trends of Oxygen Reduction Reaction for Nonaqueous Li-Air Batteries. *J. Am. Chem. Soc.* **2011**, *133* (47), 19048−19051.

(17) Mei, D.; Yuan, X.; Ma, Z.; Wei, P.; Yu, X.; Yang, J.; Ma, Z. F. A SnO_2-Based Cathode Catalyst for Lithium-Air Batteries. *ACS Appl. Mater. Interfaces* **2016**, *8* (20), 12804−12811.

(18) Li, J.; Wang, N.; Zhao, Y.; Ding, Y.; Guan, L. MnO_2 nanoflakes Coated on Multi-Walled Carbon Nanotubes for Rechargeable Lithium-Air Batteries. *Electrochem. Commun.* **2011**, *13* (7), 698−700.

(19) Majidi, L.; Yasaei, P.; Warburton, R. E.; Fuladi, S.; Cavin, J.; Hu, X.; Hemmat, Z.; Cho, S. B.; Abbasi, P.; Vörös, M.; et al. New Class of Electrocatalysts Based on 2D Transition Metal Dichalcogenides in Ionic Liquid. *Adv. Mater.* **2019**, *31* (4), 1804453.

(20) Qi, F.; Chen, Y.; Zheng, B.; He, J.; Li, Q.; Wang, X.; Lin, J.; Zhou, J.; Yu, B.; Li, P.; et al. Hierarchical Architecture of ReS_2/RGO Composites with Enhanced Electrochemical Properties for Lithium-ion Batteries. *Appl. Surf. Sci.* **2017**, *413*, 123−128.

(21) Qi, F.; Wang, X.; Zheng, B.; Chen, Y.; Yu, B.; Zhou, J.; He, J.; Li, P.; Zhang, W.; Li, Y. Self-Assembled Chrysanthemum-like Microspheres Constructed by Few-Layer $ReSe_2$ Nanosheets as a Highly Efficient and Stable Electrocatalyst for Hydrogen Evolution Reaction. *Electrochim. Acta* **2017**, *224*, 593−599.

(22) Wang, L.; Sofer, Z.; Luxa, J.; Sedmidubský, D.; Ambrosi, A.; Pumera, M. Layered Rhenium Sulfide on Free-Standing Three-Dimensional Electrodes Is Highly Catalytic for the Hydrogen Evolution Reaction: Experimental and Theoretical Study. *Electrochem. Commun.* **2016**, *63*, 39−43.

(23) Rahman, M.; Davey, K.; Qiao, S.-Z. Advent of 2D Rhenium Disulfide (ReS_2): Fundamentals to Applications. *Adv. Funct. Mater.* **2017**, *27* (10), 1606129.

(24) Fujita, T.; Ito, Y.; Tan, Y.; Yamaguchi, H.; Hojo, D.; Hirata, A.; Voiry, D.; Chhowalla, M.; Chen, M. Chemically Exfoliated ReS_2 Nanosheets. *Nanoscale* **2014**, *6* (21), 12458−12462.

(25) Gao, J.; Li, L.; Tan, J.; Sun, H.; Li, B.; Idrobo, J. C.; Singh, C. V.; Lu, T. M.; Koratkar, N. Vertically Oriented Arrays of ReS_2 Nanosheets for Electrochemical Energy Storage and Electrocatalysis. *Nano Lett.* **2016**, *16* (6), 3780−3787.

(26) Zhao, W.; Tan, X.; Jiang, J.; Liu, F.; Mu, T. Highly Efficient, Green, and Scalable β-Cyclodextrin-Assisted Aqueous Exfoliation of Transition-Metal Dichalcogenides: MoS_2 and ReS_2 Nanoflakes. *Chem. - Asian J.* **2017**, *12*, 1052−1056.

https://dx.doi.org/10.1021/acs.chemmater.9b04117
Chem. Mater. 2020, 32, 2764−2773

(27) Sahu, R.; Bhat, U.; Batra, N. M.; Sharona, H.; Vishal, B.; Sarkar, S.; Assa Aravindh, S.; Peter, S. C.; Roqan, I. S.; Costa, P. M. F. J.; et al. Nature of Low Dimensional Structural Modulations and Relative Phase Stability in Re_x $Mo(W)_{1-x}S_2$ Transition Metal Dichalcogenide Alloys. *J. Appl. Phys.* **2017**, *121* (10), 105101.
(28) Mamaca, N.; Mayousse, E.; Arrii-Clacens, S.; Napporn, T. W.; Servat, K.; Guillet, N.; Kokoh, K. B. Electrochemical Activity of Ruthenium and Iridium Based Catalysts for Oxygen Evolution Reaction. *Appl. Catal., B* **2012**, *111*−*112*, 376−380.
(29) Reier, T.; Oezaslan, M.; Strasser, P. Electrocatalytic Oxygen Evolution Reaction (OER) on Ru, Ir, and Pt Catalysts: A Comparative Study of Nanoparticles and Bulk Materials. *ACS Catal.* **2012**, *2* (8), 1765−1772.
(30) Wang, Y.; Liang, Z.; Zou, Q.; Cong, G.; Lu, Y. C. Mechanistic Insights into Catalyst-Assisted Nonaqueous Oxygen Evolution Reaction in Lithium-Oxygen Batteries. *J. Phys. Chem. C* **2016**, *120* (12), 6459−6466.
(31) Härk, E.; Jäger, R.; Kasatkin, P. E.; Möller, P.; Kanarbik, R.; Tallo, I.; Joost, U.; Aruväli, J.; Paiste, P.; Jiang, H.; et al. The Electrochemical Activity of Two Binary Alloy Catalysts toward Oxygen Reduction Reaction in 0.1 M KOH. *J. Solid State Electrochem.* **2018**, *22* (1), 31−40.
(32) Krishnamoorthy, K.; Pazhamalai, P.; Kim, S. J. Ruthenium Sulfide Nanoparticles as a New Pseudocapacitive Material for Supercapacitor. *Electrochim. Acta* **2017**, *227*, 85−94.
(33) Kratzig, A.; Zachäus, C.; Brunken, S.; Thomas, D.; Bogdanoff, P.; Ellmer, K.; Fiechter, S. RuS_2 Thin Films as Oxygen-Evolving Electrocatalyst: Highly Oriented Growth on Single-Crystal FeS_2 Substrate and Their Properties Compared to Polycrystalline Layers. *Phys. Status Solidi A* **2014**, *211* (9), 2020−2029.
(34) Hara, Y.; Minami, N.; Itagaki, H. Electrocatalytic Properties of Ruthenium Modified with Te Metal for the Oxygen Reduction Reaction. *Appl. Catal., A* **2008**, *340* (1), 59−66.
(35) Schulenburg, H.; Hilgendorff, M.; Dorbandt, I.; Radnik, J.; Bogdanoff, P.; Fiechter, S.; Bron, M.; Tributsch, H. Oxygen Reduction at Carbon Supported Ruthenium-Selenium Catalysts: Selenium as Promoter and Stabilizer of Catalytic Activity. *J. Power Sources* **2006**, *155* (1), 47−51.
(36) Müller, B.; Lutz, H. D. Raman Spectra of $MnSe_2$, $MnTe_2$, $RuTe_2$, and $OsTe_2$. *Solid State Commun.* **1991**, *78* (5), 469−471.
(37) Müller, B.; Lutz, H. D. Single Crystal Raman Studies of Pyrite-Type RuS_2, $RuSe_2$, OsS_2, $OsSe_2$, PtP_2, and $PtAs_2$. *Phys. Chem. Miner.* **1991**, *17* (8), 716−719.
(38) Huang, C. R.; Lee, M. C.; Huang, Y. S.; Lin, S. S.; Dann, T. E.; Chien, F. Z. Complete First-Order Raman Spectra of $RuSe_2$. *J. Phys. Chem. Solids* **1990**, *51* (5), 387−390.
(39) Taguchi, I.; Vaterlaus, H. P.; Bichsel, R.; Lévy, F.; Berger, H.; Yumoto, M. A Raman Scattering Study of Phonons in RuS_2 and $RuSe_2$ Single Crystals. *J. Phys. C: Solid State Phys.* **1987**, *20*, 4241−4250.
(40) Sourisseau, C.; Cavagnat, R.; Fouassier, M.; Jobic, S.; Deniard, P.; Brec, R.; Rouxel, J. The Vibrational Resonance Raman Spectra and the Valence Force Field of Iridium Dichalcogenides, IrS_2 and $IrSe_2$. *J. Solid State Chem.* **1991**, *91*, 153−172.
(41) Lazarevic, N.; Bozin, E. S.; Scepanovic, M.; Opacic, M.; Lei, H.; Petrovic, C.; Popovic, Z. V. Probing IrTe2 Crystal Symmetry by Polarized Raman Scattering. *Phys. Rev. B: Condens. Matter Mater. Phys.* **2014**, *89* (22), 224301.
(42) Qi, F.; He, J.; Chen, Y.; Zheng, B.; Li, Q.; Wang, X.; Yu, B.; Lin, J.; Zhou, J.; Li, P.; et al. Few-Layered ReS_2 Nanosheets Grown on Carbon Nanotubes: A Highly Efficient Anode for High-Performance Lithium-Ion Batteries. *Chem. Eng. J.* **2017**, *315*, 10−17.
(43) Jariwala, B.; Voiry, D.; Jindal, A.; Chalke, B. A.; Bapat, R.; Thamizhavel, A.; Chhowalla, M.; Deshmukh, M.; Bhattacharya, A. Synthesis and Characterization of ReS_2 and $ReSe_2$ Layered Chalcogenide Single Crystals. *Chem. Mater.* **2016**, *28* (10), 3352−3359.
(44) Zhao, H.; Wu, J.; Zhong, H.; Guo, Q.; Wang, X.; Xia, F.; Yang, L.; Tan, P.; Wang, H. Interlayer Interactions in Anisotropic Atomically Thin Rhenium Diselenide. *Nano Res.* **2015**, *8* (11), 3651−3661.
(45) Jariwala, B.; Voiry, D.; Jindal, A.; Chalke, B. A.; Bapat, R.; Thamizhavel, A.; Chhowalla, M.; Deshmukh, M.; Bhattacharya, A. Synthesis and Characterization of ReS_2 and $ReSe_2$ Layered Chalcogenide Single Crystals. *Chem. Mater.* **2016**, *28* (10), 3352−3359.
(46) Jariwala, B.; Thamizhavel, A.; Bhattacharya, A. $ReSe_2$: A Reassessment of Crystal Structure and Thermal Analysis. *J. Phys. D: Appl. Phys.* **2017**, *50* (4), 044001.
(47) Li, Y.; Li, N.; Yanagisawa, K.; Li, X.; Yan, X. Hydrothermal Synthesis of Highly Crystalline RuS2 Nanoparticles as Cathodic Catalysts in the Methanol Fuel Cell and Hydrochloric Acid Electrolysis. *Mater. Res. Bull.* **2015**, *65*, 110−115.
(48) Yun, X.; Wu, S.; Li, J.; Li, L.; Zhou, J.; Lu, P.; Tang, H.; Zhu, Y. Facile Synthesis of Crystalline $RuSe_2$ Nanoparticles as a Novel Pseudocapacitive Electrode Material for Supercapacitors. *Chem. Commun.* **2019**, *55* (82), 12320−12323.
(49) Gong, Q.; Zheng, J.; Wang, Y.; Gong, S.; Yang, W.; Cheng, X.; Li, H. Highly Stable and Methanol Tolerant $RuTe_2$/C Electrocatalysts for Fuel Cell Applications. *J. Electrochem. Soc.* **2018**, *165* (10), F876−F882.
(50) Fang, A. F.; Xu, G.; Dong, T.; Zheng, P.; Wang, N. L. Structural Phase Transition in $IrTe_2$: A Combined Study of Optical Spectroscopy and Band Structure Calculations. *Sci. Rep.* **2013**, *3*, 1153.
(51) Barricelli, L. B. The Crystal Structure of Iridium Diselenide. *Acta Crystallogr.* **1958**, *11* (2), 75−79.
(52) Jobic, S.; Deniard, P.; Brec, R.; Rouxel, J.; Drew, M. G. B.; David, W. I. F. Properties of the Transition Metal Dichalcogenides: The Case of IrS_2 and $IrSe_2$. *J. Solid State Chem.* **1990**, *89* (2), 315−327.
(53) Zhang, J.; Sun, E.; Feng, X.; Liu, H.; Redfern, S. A. T.; Kanchana, V.; Liu, G.; Wang, H. Phase Transition and Superconductivity in ReS_2, $ReSe_2$ and $ReTe_2$. *Phys. Chem. Chem. Phys.* **2018**, *20* (46), 29472−29479.
(54) Wildervanck, J. C.; Jellinek, F. The Dichalcogenides of Technetium and Rhenium. *J. Less-Common Met.* **1971**, *24* (1), 73−81.
(55) Furuseth, S.; Kjekshus, A.; Bergson, G.; Ehrenberg, L.; Brunvoll, J.; Bunnenberg, E.; Djerassi, C.; Records, R. The Systems Rhenium-Arsenic, Rhenium-Antimony, Rhenium-Bismuth, Rhenium-Tellurium, and Niobium-Antimony-Tellurium. *Acta Chem. Scand.* **1966**, *20*, 245−250.
(56) Corrêa, H. P. S.; Cavalcante, I. P.; Martinez, L. G.; Orlando, C. G. P.; Orlando, M. T. D. Refinement of Monoclinic ReO_2 Structure from XRD by Rietveld Method. *Braz. J. Phys.* **2004**, *34* (3b), 1208−1210.
(57) Aoki, K.; Shimomura, O.; Minomura, S. Crystal Structure of the High-Pressure Phase of Tellurium. *J. Phys. Soc. Jpn.* **1980**, *48* (2), 551−556.
(58) Shen, Y.; Fan, A.; Wei, D.; Gao, S.; Liu, W.; Han, C.; Cui, B. A Low-Temperature n-Propanol Gas Sensor Based on TeO_2 Nanowires as the Sensing Layer. *RSC Adv.* **2015**, *5* (37), 29126−29130.
(59) Singh Gaur, R. P.; Wolfe, T. A.; Braymiller, S. A. Recycling of Rhenium-Containing Wire Scrap. *Int. J. Refract. Hard Met.* **2015**, *50*, 79−85.
(60) Lu, Y.-C.; Gasteiger, H. A.; Crumlin, E.; McGuire, R.; Shao-Horn, Y. Electrocatalytic Activity Studies of Select Metal Surfaces and Implications in Li-Air Batteries. *J. Electrochem. Soc.* **2010**, *157* (9), A1016.
(61) Lu, Y.-C.; Gasteiger, H. A.; Shao-Horn, Y. Method Development to Evaluate the Oxygen Reduction Activity of High-Surface-Area Catalysts for Li-Air Batteries. *Electrochem. Solid-State Lett.* **2011**, *14* (5), A70.
(62) Li, Q.; Xu, P.; Zhang, B.; Tsai, H.; Wang, J.; Wang, H.-L.; Wu, G. One-Step Synthesis of Mn_3O_4/Reduced Graphene Oxide Nanocomposites for Oxygen Reduction in Nonaqueous Li-O_2 Batteries. *Chem. Commun.* **2013**, *49* (92), 10838.
(63) Ma, S.; Sun, L.; Cong, L.; Gao, X.; Yao, C.; Guo, X.; Tai, L.; Mei, P.; Zeng, Y.; Xie, H.; et al. Multiporous $MnCo_2O_4$ microspheres

as an Efficient Bifunctional Catalyst for Nonaqueous Li-O_2 batteries. *J. Phys. Chem. C* **2013**, *117* (49), 25890−25897.
(64) Zhao, Y.; Xu, L.; Mai, L.; Han, C.; An, Q.; Xu, X.; Liu, X.; Zhang, Q. Hierarchical Mesoporous Perovskite $La_{0.5}Sr_{0.5}CoO_{2.91}$ Nanowires with Ultrahigh Capacity for Li-Air Batteries. *Proc. Natl. Acad. Sci. U. S. A.* **2012**, *109* (48), 19569−19574.
(65) Li, Y.; Wang, J.; Li, X.; Geng, D.; Banis, M. N.; Li, R.; Sun, X. Nitrogen-Doped Graphene Nanosheets as Cathode Materials with Excellent Electrocatalytic Activity for High Capacity Lithium-Oxygen Batteries. *Electrochem. Commun.* **2012**, *18* (1), 12−15.
(66) Hung, T.-F.; Mohamed, S. G.; Shen, C.-C.; Tsai, Y.-Q.; Chang, W.-S.; Liu, R.-S. Mesoporous $ZnCo_2O_4$ Nanoflakes with Bifunctional Electrocatalytic Activities toward Efficiencies of Rechargeable Lithium-Oxygen Batteries in Aprotic Media. *Nanoscale* **2013**, *5* (24), 12115.
(67) Benck, J. D.; Chen, Z.; Kuritzky, L. Y.; Forman, A. J.; Jaramillo, T. F. Amorphous Molybdenum Sulfide Catalysts for Electrochemical Hydrogen Production: Insights into the Origin of Their Catalytic Activity. *ACS Catal.* **2012**, *2* (9), 1916−1923.
(68) Chan, K.; Tsai, C.; Hansen, H. A.; Nørskov, J. K. Molybdenum Sulfides and Selenides as Possible Electrocatalysts for CO_2 Reduction. *ChemCatChem* **2014**, *6* (7), 1899−1905.
(69) Jaramillo, T. F.; Jørgensen, K. P.; Bonde, J.; Nielsen, J. H.; Horch, S.; Chorkendorff, I. Identification of Active Edge Sites for Electrochemical H_2 evolution from MoS_2 nanocatalysts. *Science* **2007**, *317* (5834), 100−102.
(70) Huang, Y.; Nielsen, R. J.; Goddard, W. A.; Soriaga, M. P. The Reaction Mechanism with Free Energy Barriers for Electrochemical Dihydrogen Evolution on MoS_2. *J. Am. Chem. Soc.* **2015**, *137* (20), 6692−6698.
(71) Tongay, S.; Sahin, H.; Ko, C.; Luce, A.; Fan, W.; Liu, K.; Zhou, J.; Huang, Y.-S.; Ho, C.-H.; Yan, J.; et al. Monolayer Behaviour in Bulk ReS_2 Due to Electronic and Vibrational Decoupling. *Nat. Commun.* **2014**, *5*, 3252.
(72) Urushihara, M.; Chan, K.; Shi, C.; Nørskov, J. K. Theoretical Study of $EMIM^+$ Adsorption on Silver Electrode Surfaces. *J. Phys. Chem. C* **2015**, *119* (34), 20023−20029.
(73) Medina-Ramos, J.; Zhang, W.; Yoon, K.; Bai, P.; Chemburkar, A.; Tang, W.; Atifi, A.; Lee, S. S.; Fister, T. T.; Ingram, B. J.; et al. Cathodic Corrosion at the Bismuth-Ionic Liquid Electrolyte Interface under Conditions for CO_2 Reduction. *Chem. Mater.* **2018**, *30* (7), 2362−2373.

■ NOTE ADDED AFTER ASAP PUBLICATION

This paper was published ASAP on April 1, 2020, with errors in Figures 2 and 4. The corrected version was reposted on April 3, 2020.

https://dx.doi.org/10.1021/acs.chemmater.9b04117
Chem. Mater. 2020, 32, 2764−2773